# Trajectory Planning for Patch Clamp in a Highly Constrained Cerebrovascular Environment

Jie Li<sup>1,2</sup>, *Graduate Student Member, IEEE*, Zizhen Li<sup>1,2</sup>, Mingzhu Sun<sup>1,2</sup>, *Member, IEEE*, and Xin Zhao<sup>1,2,⊠</sup>, *Member, IEEE* 

Abstract—The patch-clamp technique is the gold standard for electrophysiologists' research into the cellular and molecular biological mechanisms underlying mental activities at the animal level. During the procedure, micropipette trajectory planning plays a significant role in the in vivo patch clamp. However, the high constraint between the cerebral environment and the micropipette's movement, as well as the absence of comprehensive 3D spatial information, make planning its trajectory incredibly challenging. To efficiently avoid blood vessel obstacles and insert into a target destination, this paper proposes an active avoidance micropipette trajectory planning method to improve the efficiency of the micropipette insertion process for in vivo patch clamp. More precisely, a feasible navigable space based on the available spatial information for the micropipette is first developed. The available spatial information is obtained by constructing the three-dimensional vessel distribution within the two-photon microscope imaging field of view. Based on the micropipette's navigable space, a trajectory potential field is then introduced to navigate the micropipette to the destination along the optimized trajectory. Finally, experimental validations and applications demonstrate that our proposed approach increases the success rate and reduces the execution time for the micropipette insertion, well as minimizes damage to the brain tissue.

15

20

22

24

27

34

*Index Terms*—Micropipette trajectory planning, in vivo navigation, vessel avoidance, robotic patch clamp

### I. INTRODUCTION

HE patch-clamp technique, the gold standard method for electrophysiology, enables precise analysis of ion channel activity in cells [1], [2]. It uses an electrolyte-filled glass micropipette to form a tight seal with a single cell membrane [1]. This enables accurate measurement of transmembrane voltages and intracellular currents, revealing functional responses in electrically excitable cells within their biological activities [3]. This technique has greatly advanced our understanding of cellular excitability and related physiological and pathological mechanisms [3], [4].

Despite its evident prowess, the execution of patch-clamp recordings demands a significant investment of specialized knowledge and labor [5]–[7]. The procedure necessitates meticulous manipulation of the micropipette to insert into the

<sup>1</sup>National Key Laboratory of Intelligent Tracking and Forecasting for Infectious Diseases, Engineering Research Center of Trusted Behavior Intelligence, Ministry of Education, Tianjin Key Laboratory of Intelligent Robotic (tikLIR), Institute of Robotics & Automatic Information System (IRAIS), Nankai University, Tianjin 300350, China. <sup>2</sup>Shenzhen Research Institute of Nankai University, Shenzhen 518083, China. <sup>™</sup>Corresponding author: zhaoxin@nankai.edu.cn.

This work is supported by the National Natural Science Foundation of China (62027812, 62333012).

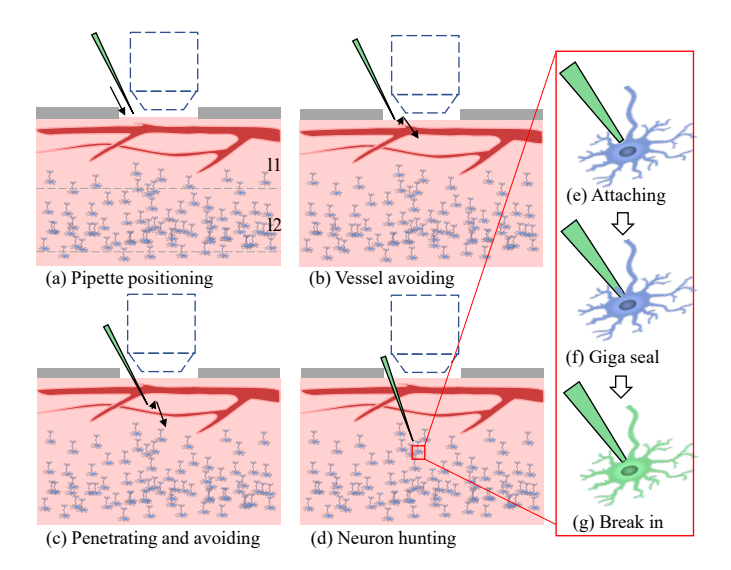


Fig. 1. Overview of the in vivo patch-clamp procedure: Conventional micropipette insertion requires careful navigation through stages (a), (b), (c), and (d), with meticulous adjustments to prevent the pipette from puncturing blood vessels. In contrast, our active avoidance trajectory planning method enables direct guidance of the micropipette from stage (a) to (d), neglecting the need for intermediately readjusting the pipette and dodging the vessels in stages (b) and (c).

42

49

51

55

brain, avoid the vessel, approach the destination, hunt and attach a target neuron, as well as form a high-resistance seal with the cell membrane (as illustrated in Fig. 1), a task that requires a high degree of technical skill and experience [7]. Besides, the success rate of the whole procedure is extremely low [8], and many attempts have failed during the initial insertion process as in Fig. 1(a)-(c). Consequently, the utilization of patch clamp, particularly its in vivo application has been embraced solely by a limited community of electrophysiologists, which has limited widespread adoption of the technique. Even for these experts, in vivo patching has relatively low data yield [8], [9]. Therefore, many attempts have been made to optimize the procedural steps associated with the patch-clamp technique, to transform it into a standardized biological tool [10]–[13].

Noting the problems associated with the trajectory planning for the in vivo patch-clamp technique, while automated in vitro patch clamp has advanced planning methods [14]–[18], technical barriers hinder their use in in vivo patch clamp micropipette insertion. A key distinction lies in the experimental environment. In in vitro patch clamp, the target specimens, such as brain slices [14] or cultured neurons [18], are isolated and maintained in a culture dish under stable, controlled conditions. Similar to micromanipulation [19], the micropipette is

125

126

127

129

131

133

135

137

141

143

145

149

152

153

154

156

158

160

164

165

166

167

169

171

174

175

176

manipulated in an unconstrained setting, free from vascular or tissue limits, enabling flexible three-dimensional navigation. These methods often seek globally optimal paths, facilitating flexible and accurate navigation, which may involve sharp turns or sudden changes in direction [18], undesirable for the delicate insertion for the in vivo patch clamp. In contrast, micropipette insertion for in vivo patch clamp occurs in a tightly constrained cranial window, limiting the movement, orientation, and visual field available for micropipette guidance [20]. Moreover, the presence of dense vasculature necessitates careful path planning to avoid collisions [21]. Although both in vitro and in vivo patch clamp are delicate cell-level operations, the dynamic and confined nature of the in vivo environment imposes far more stringent demands on trajectory planning and mechanical control.

77

79

81

82

88

101

102

103

105

107

109

111

113

114

115

116

118

120

121

Therefore, current procedures for in vivo patch clamp often rely on expert-derived heuristic trajectories that prioritize safety, minimal tissue disruption, and micropipette integrity. These methods can be categorized as "blind" and vision strategies. Specifically, Kodandaramaiah et al. [10] introduced the first automated technique of guiding a micropipette into the brain for in vivo patch-clamp recordings in anesthetized mice. This innovative approach determines the pipette's trajectory by exclusively analyzing variations in electrode impedance during the micropipette's advancement through the tissue, without microscopic imaging. Though this method emulates the fundamental procedural steps associated with the manual patchclamp experiment, its effectiveness has been demonstrated. Following their initial development, Kodandaramaiah et al. [22] extended this innovation to enable simultaneous patching of multiple cells. Desai et al. [23] described an alternative implementation of an automated micropipette insertion for patch-clamp recordings in awake, head-fixed mice running on a wheel, achieving similarly effective performance. Further, Stoy et al. [21] refined the "blind" insertion strategy by integrating automatic lateral dodging navigation, which detects and navigates around vascular obstructions, thereby reducing pipette clogging and reaching the thalamic neurons. Li et al. [24] proposed a semi-active micropipette positioning method for the deep layer of the brain, by passively sensing the pipette's resistance and actively verifying action potentials to detect neurons.

To enhance the success rate of whole-cell recordings and address the lack of selectivity inherent in "blind" patching techniques, two-photon microscopy has been integrated as vision guidance. Long et al. [11] proposed an adaptive pipette positioning strategy that utilizes three-dimensional image data, acquired at an intermediate location along the trajectory to the target, to facilitate the micropipette's navigation toward a userselected position. This method involves manually identifying the locations of the pipette tip and target to allow adaptive adjustments to the pipette's trajectory, thereby enhancing precision in positioning the tip near the target. Subsequently, Annecchino et al. [12] and Suk et al. [13] each contributed independent advancements in micropipette trajectory planning for the automation of a two-photon image-guided patch-clamp platform, designed for tracking and automated navigation toward specific targets. These platforms employ closed-loop imaging, enabling continuous adjustment of the pipette trajectory in response to the dynamic changes in target position during the insertion procedure. Furthermore, Wei et al. [25] proposed a deep-learning method to facilitate multipipette realtime localization, guiding the micropipette insertion for robotassisted in vivo patch-clamp.

Despite the progress made by the previously mentioned methods for automating the patch-clamp procedure, research concerning the trajectory of micropipette insertion is still in its nascent phase, characterized by researchers' experience and the utilization of passive penetration strategies. In the "blind" strategies, for example, the indication that the micropipette has encountered the target cell or vessel barrier is deduced from a rise in resistance [21], which often leads to withdrawing and readjusting of the micropipette's position. In the visually guided strategy, the mimicking manual operation leads the micropipette's trajectory to be continuously updated online during each focal plane advancement, requiring constant readjustment [12], [13]. Moreover, the navigational challenges posed by cerebrovascular impediments, which are ubiquitous in the brain and hinder in vivo patch-clamp experiments, have not now been extensively explored. Supplementary Table S1 provides a summary of trajectory planning methods of micropipette insertion for the robotic in vivo patch clamp.

In this study, we aim to enhance micropipette penetration efficacy for in vivo patch-clamp procedures by deploying a more sophisticated trajectory strategy. We propose a novel trajectory planning method for actively avoiding cerebrovasculature during the micropipette insertion into the brain. This approach involves introducing a feasible navigable space and a trajectory potential field to derive an optimized trajectory that guides the pipette to its destination within the brain. To be specific, the feasible navigable space for the micropipette is defined by leveraging available spatial information and the motion constraints of the micromanipulator within the imaging window of the two-photon microscope, in which the available spatial information is constructed by delineating the distribution of blood vessel obstacles, facilitating effective navigation during the insertion process. Subsequently, artificial potential fields are introduced to guide the micropipette in navigating in the feasible space, thereby deriving an optimized trajectory for the micropipette to reach the target depth. To substantiate the efficacy of the proposed method, experimental validations and applications have been conducted to demonstrate its advantages. The contribution of this article can be summarized as follows:

- A novel micropipette trajectory planning method is designed to actively avoid the vessel obstacle for the in vivo patch-clamp procedure and then accelerate the inserting process.
- A feasible navigable space and a trajectory potential field are proposed to guide the micropipette inserting into a destination of the rodent brain.
- Experiment results demonstrate that our proposed method dramatically decreases the experiment execution time and minimizes damage to the brain tissue. The method is designed to be compatible with existing hardware, allowing for straightforward application to various patch-

234

236

237

238

239

241

243

245

247

249

251

252

253

254

255

256

258

260

262

264

266

268

269

273

274

clamp systems without the need for modifications.

# II. PROBLEM ANALYSIS AND MICROPIPETTE TRAJECTORY SCHEME DESIGN

#### A. Problem Analysis of the Pipette Penetration

181

182

183

184

185

186

188

190

191

192

194

195

196

197

198

199

200

201

202

203

205

207

209

211

213

214

215

216

217

218

220

222

224

226

In the context of in vivo patch-clamp recordings, the procedure initiates with a craniotomy, which involves creating an opening in the skull to provide access to the brain—a step constrained by the requirement for a cranial window. Following the establishment of the cranial window, a micropipette is meticulously inserted through this opening toward the designated target region, as illustrated in Fig. 1(ad). Subsequent steps include attaching the pipette to the neuronal cell membrane, forming a tight seal, and rupturing the membrane to access the cell's interior, as depicted in Fig. 1(d-f). During the insertion of the micropipette into the brain, it initially traverses Layer 1 (L1), situated within  $0-100~\mu m$  beneath the cortical surface. L1 is predominantly characterized by large blood vessels, necessitating extreme caution to prevent vascular damage—a limitation referred to as the vessel constraint. The pipette then advances into Layer 2 (L2), located between 100–200  $\mu m$  in depth, where neuronal cells are densely populated. Navigating through L2 requires precise maneuvering around blood vessels to avoid puncturing them, which could result in clotting of the pipette tip and bleeding. Such complications would necessitate the termination of the current procedure and the identification of a new, undamaged brain region to recommence the experiment. Additionally, the movement of the micropipette inherently causes irreversible damage to the brain tissue. Specifically, lateral or vertical advancements produce a large shear crosssection, thereby reducing their feasibility unless necessary. This consideration is referred to as the movement constraint. Considering a general situation, the tip of a micropipette is inserted into the brain, guided by a certain trajectory planning strategy f:

$$p(x, y, z) = f(x, y, z) \tag{1}$$

Where  $z \in (0,100\mu m(target\ depth))$  is the inserting depth, p(x,y,z) is the tip's location within the cranial window. When the patch-clamp procedure is performed blindly, practitioners often rely on changes in pipette resistance to detect physical impediments like blood vessels during the insertion:

$$p(x, y, z) = f(\Omega(x, y, z)) \tag{2}$$

Where  $\Omega(x,y,z)$  is the pipette resistance in location (x,y,z). However, this approach only identifies obstacles at the current location of the pipette, leaving uncertainty about potential barriers in the surrounding and deeper tissue. This limitation introduces complexity in determining an optimal insertion trajectory, as the structural environment of the brain dictates how the pipette must be maneuvered. On the other hand, employing two-photon microscopy offers the advantage of real-time visualization during pipette insertion:

$$p(x, y, z) = f(V_{win}^z) \tag{3}$$

Where  $V_{win}^z$  is the imaging window of the microscope in the focus plane z. However, due to the inherent nonlinearity [26]

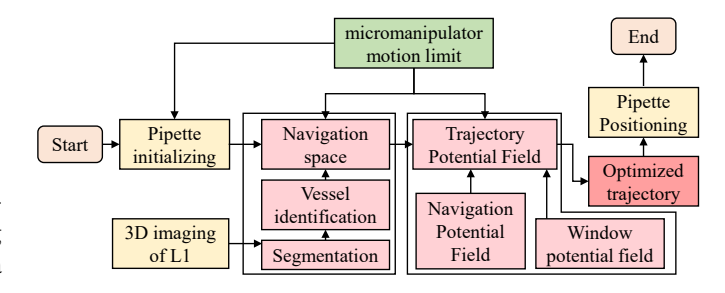


Fig. 2. Flowchart of the proposed active micropipette trajectory planning.

of two-photon imaging, it restricts visualization to a limited focal plane, rendering areas outside of the focal zone invisible. This opacity requires continuous adjustments to the pipette's path as the image field updates, making it necessary to adapt the trajectory dynamically to accommodate the information provided by the constantly shifting focal environment. Consequently, while two-photon microscopy offers superior spatial resolution, it also introduces challenges in maintaining an accurate trajectory through complex brain structures.

# B. Basic Idea of the Proposed Trajectory Planning Method

To address the challenges associated with micropipette trajectory planning during in vivo patch-clamp procedures and to streamline this process into a standardized protocol, we propose an active trajectory planning method for precise pipette insertion into the brain. Our approach consists of a two-phase strategy designed to enhance both the safety and efficiency of micropipette navigation. In the first phase, we focus on constructing a feasible navigable space within the brain by leveraging existing spatial data from the imaging window. This spatial information is augmented through the use of fluorescent labeling, which enhances the visibility of key anatomical features. Subsequently, a three-dimensional (3D) map of the brain's vascular architecture is generated. Given the potential for noise and artifacts in two-photon imaging, where vessels and surrounding tissue may become indistinguishable, we incorporate an efficient vessel segmentation method to differentiate blood vessels from the background tissue accurately. This segmentation is critical to ensure a clear representation of the brain's vasculature, thus aiding in the identification of a safe trajectory. In the second phase, we introduce a trajectory potential field to optimize the micropipette's insertion path. This field integrates a navigation potential field, which governs the movement of the pipette based on the 3D vascular map, and a window potential field, which defines the spatial constraints of the imaging area. These fields are coupled with the mechanical motion constraints of the micromanipulator used to control the pipette, ensuring that the trajectory adheres to the physical limitations of the system. The result is an optimized insertion path that minimizes the risk of vessel puncture and the complexity of the trajectory. Finally, the optimized trajectory is used to automate the pipette insertion process, guiding it to the desired target position within the brain. The flowchart of the proposed method is shown in Fig.

331

332

334

336

337

339

341

343

345

347

349

351

353

354

358

# III. MICROPIPETTE TRAJECTORY PLANNING AND ANALYSIS

#### A. Micropipette Feasible Navigable Space

275

276

277

279

282

283

284

285

287

288

289

291

293

294

295

296

297

298

299

300

301

302

303

304

306

308

309

310

311

312

313

314

315

317

319

321

323

325

326

327

According to the equation 1, the trajectory planning is to find a strategy f to narrow the position of the micropipette within the imaging window to obtain the optimized path:

$$P(x, y, z) = \{ \underset{p(x, y, z)}{\arg \min} f(V_{win})$$

$$\mid p(x, y, z) \in V_{win}, z \in (0, 100 \mu m) \}$$
(4)

where P(x,y,z) is the optimized path. Considering that micropipette insertion is a 3D spatial process, rather than relying solely on on-focus plane information during pipette advancement, as is done in conventional methods, we utilize the full 3D spatial information as a priori knowledge. This allows for a more comprehensive understanding of the surrounding anatomical structures and enables more accurate and informed trajectory planning throughout the insertion process.

The 3D spatial information necessary for planning micropipette insertion can be obtained by acquiring an imaging stack of L1, as shown in Fig. 3(a) and Supplemental Fig. S4. Since large blood vessels are predominantly distributed within L1 of the mouse brain, and neuronal cells are concentrated in L2, capturing spatial information for L1 is sufficient for avoiding vessels during the insertion process. This focused acquisition of L1 minimizes the time required for image collection while still providing the essential data for vessel avoidance. Once the imaging data is obtained, the vessel distribution can be constructed. This step is crucial for identifying vessel-free regions and ensuring a safe insertion path for the micropipette. However, accurately discerning vascular structures from the background presents significant challenges due to the inherent detection noise in two-photon imaging. Traditional computer vision techniques, such as edge detection, histograms or the Otsu thresholding method, often struggle to effectively differentiate between vessels and surrounding tissue in a noisy imaging environment.

To overcome the limitations of traditional methods, we use a deep learning network [27] to accurately segment 3D vascular structures from noisy two-photon microscopy images. The network employs a U-shaped encoder-decoder architecture, a proven framework for multi-scale feature extraction in biomedical image segmentation. Its core is a "guard-laborer" structure, where a Swin Transformer (the guard) captures global context and a 3D CNN (the laborer) extracts local features. The encoder path uses these modules and a bottleneck Swin Transformer to downsample features to 1/32 of the original image resolution. The decoder path reverses this structure, using skip connections to ensure each "laborer" module receives guidance from both an encoder and a decoder "guard." Finally, these nested features are fed into a terminal 3D CNN block to generate the segmented image. A comprehensive description of the network is provided in [27]. Here, we employ the network for brain vessel segmentation shown in Fig. 3(b) and Supplementary Fig. S4.

In the context of 3D spatial planning for micropipette insertion, the candidate space for safe insertion into the brain can

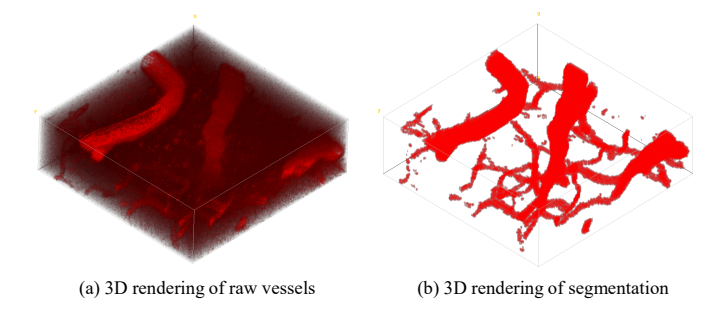


Fig. 3. Example of (a) the cerebrovasculature from a mouse acquired by a two-photon microscope and (b) the corresponding segmentation.

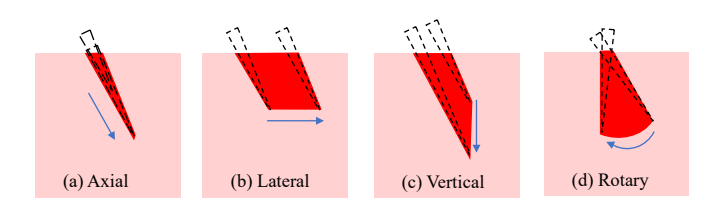


Fig. 4. Illustration of the contact areas (red areas) between the brain (pink rectangle) and the micropipette (dotted black triangle) as it advances the same distance within the brain tissue along (a) axial, (b) lateral, (c) vertical, and (d) rotary directions.

be mathematically described using the 3D imaging window,  $V_{win}$ , and the 3D vessel distribution,  $V_{vessel}$ . The available background environment, which represents the candidate navigable space  $V_{env}$  for micropipette insertion, can be expressed as:

$$V_{env} = V_{win} - V_{vessel} \tag{5}$$

When considering in vivo micropipette insertion, the procedure is governed by the constraints of the micromanipulator, which controls the micropipette's movement. The increased degrees of freedom provided by the micromanipulator introduce greater complexity to the insertion trajectory. While enhanced flexibility is advantageous for navigating around vessels and other structures, it also increases the risk of brain tissue damage. The trajectory's complexity and the associated contact surfaces between the micropipette and brain tissue directly influence the extent of mechanical disruption. As illustrated in Fig. 4, the contact surface between the micropipette and the brain tissue varies depending on the direction of insertion when the pipette advances the same distance. This underscores the importance of optimizing the insertion trajectory to minimize tissue disruption while ensuring safe navigation. It is evident that axial motion during micropipette insertion into the brain significantly reduces the contact surface between the pipette and the brain tissue, as the interaction is confined primarily to the pipette's cross-sectional area. In contrast, motion along other degrees of freedom introduces a shearing effect, which increases the contact surface area due to lateral or angular displacement. This shearing action can cause greater disruption and deformation of the surrounding tissue. Cumulatively, trajectories with more complex or curved pipette motion action result in dramatically increased surface contact, potentially leading to greater tissue deformation or damage. To incorporate this understanding into our methodology, we

411

413

415

416

417

418

419

420

422

423

424

425

426

427

429

430

431

432

434

435

436

438

439

440

propose micromanipulator motion constraints specifically designed to reduce tissue damage during in vivo micropipette insertion for patch-clamp experiments. The constraints are defined based on the depth of the micropipette tip relative to the brain surface:

361

362

363

364

366

367

368

370

372

373

375

377

378

379

380

382

383

384

385

386

387

388

389

390

391

392

393

394

395

396

397

399

401

403

406

$$M_{tip} = \begin{cases} free, & \text{if } depth > 0\\ axial, & \text{if } depth \le 0 \end{cases}$$
 (6)

free indicates that the micropipette is unrestricted in its movement, allowing full degrees of freedom when the tip is positioned above the brain tissue (i.e., when depth>0). In this region, the pipette can be maneuvered freely, allowing for flexible alignment and approach. However, once the micropipette tip enters the brain tissue ( $depth \leq 0$ ), motion is restricted to the axial direction, limiting displacement to longitudinal advancement along the pipette's axis.

Next, by applying the movement constraint  $M_{tip}$  to the candidate space  $V_{env}$ , we define the navigation space  $V_{navg}$  for micropipette insertion. This space represents the region where the pipette can navigate within the brain while adhering to the movement constraints:

$$V_{navg} = V_{env} \otimes M_{tip}$$

$$= (V_{win} - V_{vessel}) \otimes M_{tip}$$
(7)

where  $\otimes$  denotes the application of the motion constraint to the candidate space. In this formulation, the candidate space  $V_{env}$ , which excludes regions occupied by blood vessels, is further refined by the constraints imposed by  $M_{tip}$ . Specifically, when the micropipette tip is above the brain tissue, its motion is unconstrained, meaning the tip can freely traverse this space. In practice, this is relatively simple, as the shortest path between two points is a straight line. Thus, the primary focus is on the constrained navigation within the brain tissue itself, where axial motion is required to minimize tissue damage. The visualization of the candidate space and the navigation space of the micropipette is shown in Fig. 5. In Fig. 5(a), the candidate space represents the unconstrained feasible region for pipette insertion, excluding blood vessels but allowing free movement in all directions. However, in Fig. 5(b) the navigation space reflects the feasible insertion domain when the axial motion constraint is applied. This demonstrates a significant reduction in the available navigable region compared to the broader candidate space. As shown in Fig. 5(c), the navigation space does not permit arbitrary movement throughout the entire 3D volume. Instead, it restricts the pipette's insertion from the surface to the target endpoint along an axial trajectory. This axial-only motion, enforced once the micropipette enters the brain tissue, ensures that the insertion process minimizes lateral displacement, thereby reducing the risk of damage to surrounding structures.

B. Trajectory Potential Field for Micropipette Optimized Trajectory

Based on the proposed navigation space, the equation 4 governing micropipette trajectory selection can be formulated

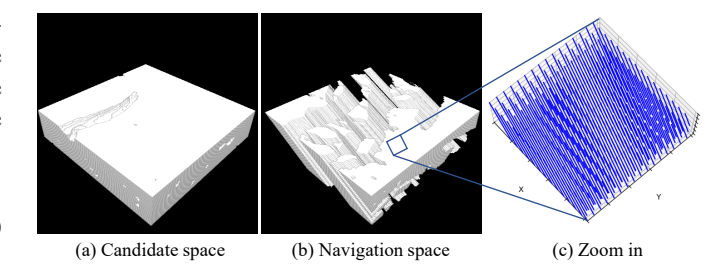


Fig. 5. Visualization of (a) candidate space and (b) navigation space for in vivo insertion of the micropipette. (c) is the zoom-in view of the blue square in (b).

as follows:

$$P(x, y, z) = \{ \underset{p(x, y, z)}{\arg \min} f(V_{navg})$$

$$\mid p(x, y, z) \in V_{navg}, z \in (0, 100 \mu m) \}$$

$$(8)$$

Within the navigation space, numerous potential trajectories exist for micropipette insertion, as illustrated in Fig.5(b). It is necessary to automatically screen and select the optimal trajectory among the candidate trajectories. We introduce a navigation evaluation function f that maps the navigation space  $V_{navg}$  into an evaluative measure  $f(V_{navg})$ , and obtain the values of f. The optimal path is then obtained by selecting the minimum value of this function. Thus, the design of an effective evaluation function f becomes a key element of the process. Here, the artificial potential field (APF) is employed to facilitate the automatic identification and positioning of the optimized trajectory.

1) Navigation Potential Field: Within the navigation space, the boundary lies close to vascular obstacles. Additionally, brain fluctuations also account for the potential discrepancies in the boundary. To mitigate the risk of vascular puncture, a buffer zone is established around this boundary. The buffer zone can be established by erosion operations in the navigation space:

$$V'_{navq} = V_{navq} \ominus E \tag{9}$$

where  $V'_{navg}$  is the refined navigation space,  $\ominus$  denotes the erosion operation, and E is the erosion factor that determines how much the navigation space is reduced. And E should be larger than the fluctuation range. This step ensures that regions too close to blood vessels are excluded from potential trajectories, reducing the risk of vessel puncture.

Once the refined navigation space is defined, we establish a Navigation Potential Field (NPF) using a Gaussian function to guide the micropipette toward the optimal path:

$$G(x, y, z) = \begin{cases} Ae^{-\frac{r_z^2}{2c^2}}, & \text{if } r < R\\ 0, & \text{otherwise} \end{cases}$$
 (10)

Where A is the amplitude,  $r_z = \sqrt{x^2 + y^2}$  represents the detection distance, R is the detection range, and  $c \in \mathbb{R}$  denotes the standard deviation. Finally, the NPF is obtained by combining equation 7, 9 and 10:

$$F_{navg}(x, y, z) = G(x, y, z) * V'_{navg} + \alpha V_{navg}$$
 (11)

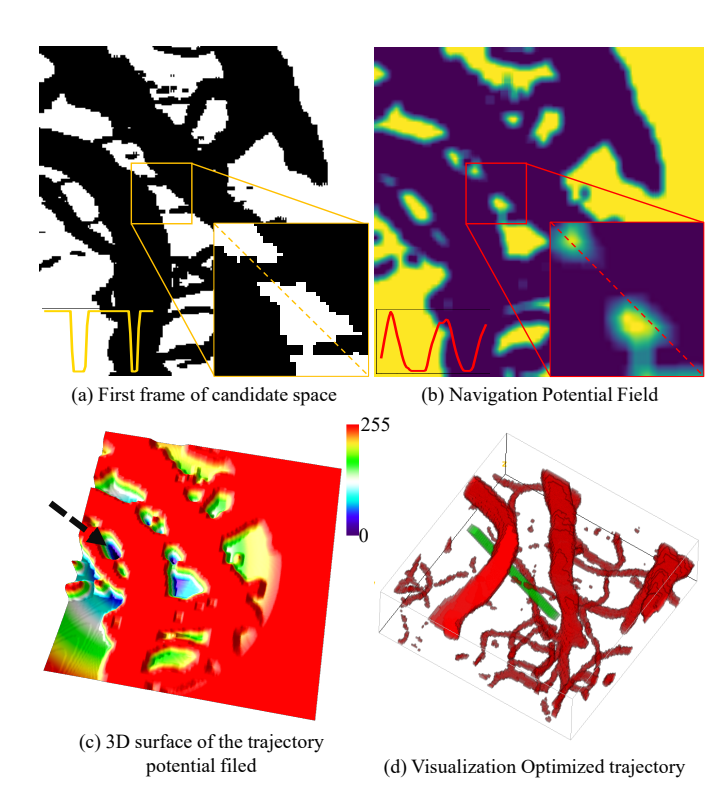


Fig. 6. (a) The candidate space. (b) The navigation potential field. The curves at the bottom left in (a) and (b) are the pixel value traces of the yellow and red dashed lines in the insert zoom-in pictures, respectively. (c) The trajectory potential field (TPF) determines the insertion coordinates by selecting the position with the minimum TPF value (as indicated by the dashed arrow). (d) The visualization of the optimized trajectory in the 3D vessel distribution.

Where  $\alpha \in (0,1)$  is the scale factor that balances the influence of the refined navigation space  $V_{navg}^{\prime}$  and the broader navigation space  $V_{navg}$ . The visualization of the NPF is illustrated in Fig. 6(b). Compared to the candidate space in Fig. 6(a), the NPF significantly reduces the feasible domain, particularly in regions where the micropipette might accidentally puncture blood vessels. The erosion operator eliminates high-risk areas close to vessels, while the Gaussian function creates a gradient that favors insertion points at the center of the remaining feasible region. This ensures that the micropipette is continually guided toward the most favorable insertion path, minimizing the risk of accidental vessel damage. By incorporating the NPF, we achieve a more controlled and reliable navigation space for micropipette insertion. The gradient formed by the NPF serves as a guiding force, ensuring that the micropipette follows a path that avoids blood vessels when proceeding with the pipette insertion.

2) Window Potential Field: To effectively guide the micropipette along a safe insertion path, it is also crucial to maintain the tip within the FOV as much as possible. In manual operation, operators typically adjust the imaging window to center the micropipette tip in the FOV, as this positioning not only enhances control and visibility but also aligns with operator preferences in in vivo patch-clamp procedures. However, in our automated procedure, continuously adjusting the imaging window to center the tip would require recalculating the navigation space for each new view, imposing significant computational and time burdens. To facilitate this, we fix

the imaging window, and introduce a Window Potential Field (WPF), which models a gradual energy dissipation from the given point of the imaging window toward the periphery. In this model, the energy is maximized at the given point and decreases as the distance from the center increases. This approach ensures that the micropipette is drawn toward the central area of the FOV, reducing deviations toward the edges, which could compromise accuracy or visibility:

$$F_{win}(x, y, z) = 1 - \beta \sqrt{(x - x_{c|z})^2 + (y - y_{c|z})^2}$$
 (12)

Where  $F_{win}(x,y,z)$  is the potential value at a point (x,y) within the imaging window at depth z, The parameter  $\beta$  denotes the weight factor that controls the rate of energy dissipation, the weight factor governing the rate of energy dissipation, which determines the rate at which the potential decreases as the distance from the center increases. The given point  $(x_{c|0},y_{c|0})$  is set to approximately one-quarter of the imaging window's dimension, ensuring that the micropipette tip remains within the FOV as it approaches the target layer. This setup creates a "gravitational pull" effect, where the micropipette tip is naturally attracted to the center of the window, ensuring that the insertion path remains focused in the central region of the imaging window.

3) Trajectory Potential Field: To finalize the trajectory planning for the micropipette insertion, the objective function f is formulated by combining equation 11 and 12, and we call it the trajectory potential field (TPF):

$$f = V_{cons} - F_{win}(x, y, z) * F_{navg}(x, y, z)$$
  
=  $V_{cons} - F_{win}(x, y, z) * (G(x, y, z) * V'_{navg} + \alpha V_{navg})$   
(13)

Where  $V_{cons}$  is a constant factor and set to 255. Given the motion constraint of the micropipette during insertion into the target layer, the implementation of the equation 13 can be simplified as follows:

$$f(x, y, 0) = V_{cons} - F_{win}(x, y) * (G(x, y) * V'_{navg} + \alpha V_{navg})$$
(14)

The simplification is feasible due to the motion constraint that governs the micropipette's axial progression during insertion. And, the initial frame of the refined navigation space captures the entirety of feasible regions required, rendering it sufficient to utilize only the initial frame of both the WPF and NPF for the TPF computation.

The visualization of the TPF is depicted in Fig. 6(c), demonstrating how the fields interact to create an optimal insertion pathway. The NPF ensures that the micropipette is steered away from vascular structures, while the WPF keeps the insertion aligned toward the center of the FOV. By combining these two potential fields, the TPF creates a comprehensive gradient that directs the micropipette tip along the safest and most efficient path to the target location. Then, the final optimized trajectory is illustrated in Fig. 6(d).

To validate the effectiveness of our proposed trajectory planning algorithm, we compared our method against 3 popular trajectory planning algorithms (genetic algorithm (GA) [28], A\* algorithm [29], and rapidly-exploring Random Tree Star (RRT\*) [30]) in a simulated environment. The results

560

562

563

565

567

569

573

577

580

581

582

584

586

588

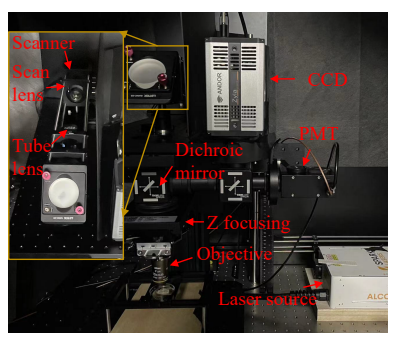
590

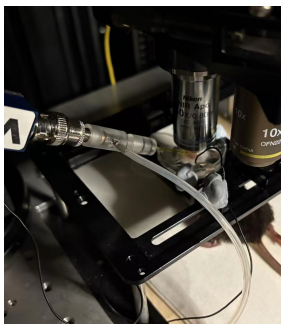
592

594

595

599





(a) Two-photon microscope

519

520

522

523

524

525

526

527

529

531

533

535

537

539

541

542

545

547

549

551

552

554

555

556

557

(b) In vivo experiment

Fig. 7. (a) The DIY two-photon microscope, including a 920 nm femtosecond laser source, scanner, scan lens, tube lens, z focusing, objective, and PMT, *etc.* (b) A snapshot of an in vivo experiment.

(Supplementary Fig. S2) demonstrate that our proposed planning algorithm has the best computational efficiency and path optimality.

#### IV. EXPERIMENTS AND APPLICATIONS

In the experiments and applications, the proposed trajectory planning method is applied to a customized in vivo patch clamping system. This system features a DIY two-photon microscope designed for high-resolution in vivo imaging and a micromanipulator that enables precise control of micropipette movement. The two-photon microscope is equipped with a 920 nm femtosecond laser as the excitation source, enabling deep tissue penetration. The microscope also includes a scanner that directs the laser in a scanning pattern, along with a scan lens, tube lens, and objective lens to ensure accurate focusing. Fluorescence emitted from the tissue is detected using a highly sensitive GaAsP photomultiplier tube (PMT), while a motorized focusing module provides depth-resolved imaging by adjusting the focal plane within the tissue. The spatial resolution is with lateral 0.72  $\mu m$  and axial 4.78  $\mu m$ (Supplementary Fig. S1). And the frame rate is with around 2 Hz with  $512 \times 512$  pixels. Figure 7 and Supplementary Fig. S9 show the DIY two-photon microscope for in vivo patch clamp experiments. The patch-clamp head can be readily installed on the micromanipulator positioned on the stage. Since the proposed method does not require any changes to the system hardware, other systems equipped with the aforementioned components can also be feasible to apply.

#### A. Implementation Details

The segmentation of 3D vessels is obtained using an NVIDIA GeForce RTX 3090 GPU. For those who lack GPU resources, a lightweight network (2D UNet) is recommended to reduce computational demands. The navigation space and the trajectory potential field are obtained based on CPUs. In our experiments, the erosion factor E is 10, the detection range R is  $\sqrt{50}$ , the scale factor  $\alpha$  is 0.2, and the weight factor  $\beta$  is set to 1.8 over the image size. As for registering the micropipette to the two-photon imaging field, we define the imaging field as the global coordinate system. We manually move the micropipette into view and align it with the imaging focal plane at the cortex surface. For xy registration, we

TABLE I
QUANTITATIVE RESULTS OF THE MICROPIPETTE INSERTION IN IN VITRO
ENVIRONMENT

EXP.		1	2	3	4	5
Conv.	TC	2	2	1	1	2
	TL	166.91	-	169.54	160.81	-
	CSA	511.96	-	814.03	221.72	-
	PB	0	1	0	0	1
	Time	63.1	-	42.6	89.1	-
Ours	TC	0	0	0	0	0
	TL	155.73	155.73	155.72	155.95	155.94
	CSA	155.73	155.73	155.72	155.95	155.94
	PB	0	0	0	0	0
	Time	10.9	10.9	11.5	11.4	11.9

manually select the pipette tip in the imaging field as its position.

#### B. In Vitro Experiments and Analysis

To quantitatively evaluate the efficiency of our proposed trajectory planning method compared to conventional visionguided micropipette insertion techniques in a controlled environment, we first conduct the pipette insertion procedure within an artificial in vitro setup. According to a reference vessel map of a mouse [31] (Supplementary Fig. S5), the vessels are randomly distributed, with a main distribution pattern of being cross, parallel, or stacked. The vessel diameter differs from large in the shallow layer of the brain to small in the deep layer. Then, we made a simulated environment as illustrated in Supplementary Fig. S5. The in vitro environment employs polyvinylidene fluoride-co-hexafluoropropylene (PVDF-HFP) microtubes, which have approximately 60 to 90 µm diameters, to replicate the blood vessels' structural complexity. These microtubes are carefully interwoven to form an intricate network and are subsequently placed within a chamber constructed from a centrifuge tube. The microtubules are then stabilized, and fluorescent dyes are injected into their interiors. Finally, the chamber is filled with either water or artificial cerebrospinal fluid (ACSF) to create a medium for micropipette navigation. An example of two-photon imaging of the microtubules and the actual cerebrovasculature of rodent cortex is illustrated in Fig. 8 (a) and Fig. 8 (b), respectively. Our in vitro environment satisfies the distribution of the vessel in Fig. 8 (b), except for the diameter variance. Yet, the diameter's influence is negligible and has no discernible effect on the overall experiment. For imaging during in vitro experiments, the laser power of the two-photon microscope is adjusted to a range of 30 to 80 mW. This power level enables high imaging quality while minimizing the risk of photobleaching, ensuring consistent observation of the micropipette's trajectory through the simulated vascular network.

Figure 9 illustrates the results of in vitro experiments, illustrating the trajectory of the micropipette tip as it traverses from the initial position to the intended depth. We performed five experiments utilizing our novel method and the conventional vision-guided approach, respectively. In comparison with the conventional approach, the proposed trajectory method provides a trajectory that is both the most straightforward and the shortest. Its proactive vessel avoidance capability eliminates

651

653

655

657

659

663

665

666

668

670

672

674

678

681

683

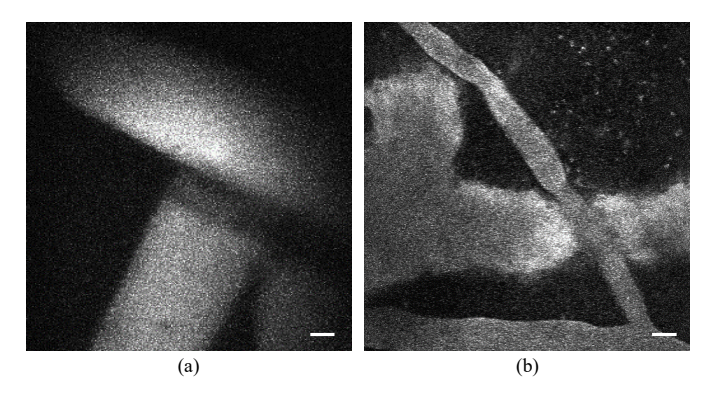


Fig. 8. Max projection of (a) PVDF-HFP microtubules image obtained by two-photon imaging. Scale bar 25  $\mu m$ , and (b) Brain vessel image of a mouse acquired by two-photon imaging. Scale bar 25  $\mu m$ .

the necessity for directional adjustments during the insertion. Conversely, the conventional strategy suffers from the "a man walking in the dark road" predicament, necessitating redirection of its insertion path to circumvent obstacles passively and to accommodate an evolving environment.

602

604

605

606

607

609

611

613

615

617

618

619

620

621

622

624

626

628

630

632

634

635

636

637

639

641

To comprehensively assess the performance and reliability of the proposed trajectory planning method, the following quantitative metrics are introduced: 1) Trajectory Complexity (TC): This metric assesses the geometric complexity of the micropipette's path by measuring directional changes along the trajectory. A higher frequency of directional changes indicates greater complexity and may imply a higher tissue impact. 2) Trajectory Length (TL): This measures the total distance traveled by the micropipette tip from the initial point to the target, serving as an indicator of procedural efficiency and path directness. A shorter trajectory length is preferred for minimizing insertion time and tissue disturbance. 3) Crosssectional Area (CSA): This metric quantifies the area of tissue intersected by the micropipette, providing insights into the spatial extent of potential tissue disruption caused by the insertion process. CSA consists of two parts: axial TL and cross area due to the directional change of the micropipette. Lower CSA values reflect reduced tissue damage (Supplementary Fig. S3). 4) Pipette Insertion Time: The time taken from insertion initiation to reaching the target depth, reflecting the method's operational speed and efficiency. A shorter insertion time is indicative of a more streamlined and effective trajectory. Note that our proposed trajectory planning method operates offline, the image acquisition, vessel segmentation, and TPF times are not included in this time metric. Image acquisition takes around 30 seconds, and our offline algorithm complete within 8.56 seconds, including 8 seconds for vessel segmentation, and 0.56 seconds for the trajectory potential field. 5) Blockage Statistics: This metric tallies instances of micropipette clogging or blockages during insertion, essential for evaluating the consistency and reliability of the method under real conditions. 6) Pipette Broken (PB): Specific to in vitro applications, this metric counts if the occurrence of micropipette tip breakage, is primarily relevant due to the rigidity of PVDF-HFP microtubes, which lack elasticity. This can reflect the excessive contact between the micropipette and these rigid microtubes which can result in tip breakage.

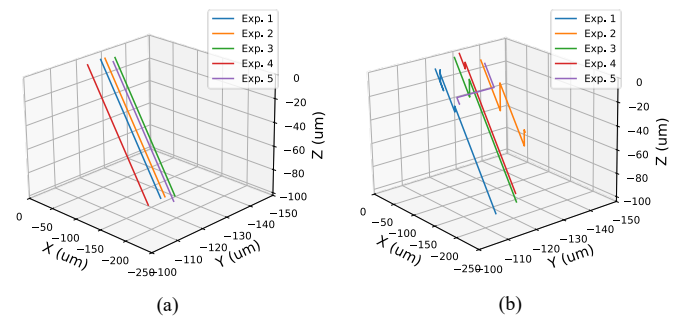


Fig. 9. The micropipettes' trajectories from in vitro experiments by (a) our and (b) conventional methods, respectively.

Table I shows a comparative assessment of the proposed trajectory method and the conventional approach, respectively. The active strategy employed by the proposed method results in the minimal TC, with a consistent value of zero across 5 experimental trials. Our method also achieves the shortest TL to target the designated position. In contrast, the conventional method exhibits a higher TC, which fluctuates in response to variations in the environmental context. The TL observed in the conventional method is subject to change. These results indicate that the proposed method exhibits a high degree of robustness and fidelity, consistently maintaining optimal performance across various experimental conditions. In terms of CSA, our approach consistently yields minimal area compared to the conventional approach, suggesting a more precise and focused trajectory through the navigation space. Conversely, the conventional method results in the largest CSA, which correlates positively with TC. In addition, our method consistently results in zero PBs across five experiments, in contrast to the conventional approach, which incurred two PBs out of five trials. This disparity arises primarily due to the differing interactions between the micropipette and the VDF-HFP microtubules. The VDF-HFP microtubules exhibit a relatively high rigidity compared to natural vessels. In the conventional method, the micropipette must employ lateral dodging to avoid contact with these microtubules, which the base of the pipette inevitably comes into contact with the microtubules, shearing occurs between them, and exceeds the bending threshold of the pipette, resulting in the breakage of the micropipette. The results demonstrate the superiority of our method, as it effectively prevents any part of the micropipette from directly contacting obstacles, thereby avoiding contactinduced damage to the micropipette. Furthermore, the duration time required for micropipette insertion using our method is significantly reduced, exceeding 4 times less than that of the conventional method. This enhancement in efficiency indicates that our approach not only optimizes the trajectory but also expedites the insertion process, which can be particularly beneficial in reducing procedural time and associated risks.

#### C. In Vivo Experiments and Analysis

Following the successful in vitro validation of the performance of our proposed trajectory planning method, we further extended its application to an in vivo environment

710

711

715

722

726

730

732

734

741

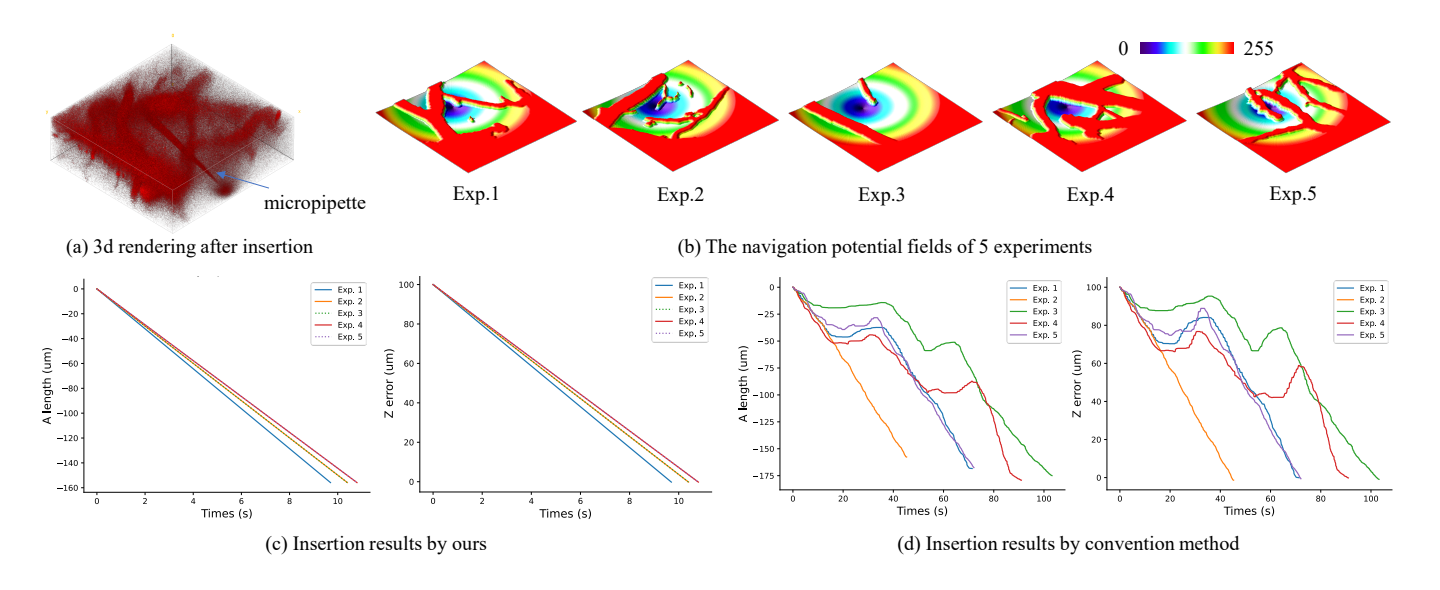


Fig. 10. (a) 3D rendering after insertion of Exp.4 using our proposed method. (b) The navigation potential fields of 5 experiments from different cerebral environments. (c) Position errors between the micropipette tip position and the destination using our method. (d) Position errors between the micropipette tip position and the destination using the conventional method.

in the mouse brain. Experiments were conducted on 6-weekold female C57BL/6J mice. A craniotomy was performed first before insertion of the micropipette into the brain. The mice were initially anesthetized and placed on a heating pad to maintain body temperature, with an ocular ointment applied to protect their eyes. The scalp was carefully dissected to expose the skull, after which a custom-designed recording chamber was affixed to the skull using adhesive and dental cement. The cement was allowed to be set for 20 minutes, after which an approximate 3 mm diameter cranial window was created using a trephine drill. The skull disc was removed with tweezers, and the dura mater was delicately excised. Agarose gel (1%) could be applied to the cranial window to decrease vessel fluctuation [24]. The fluorescent solution was then administered to the vessel via tail vein injection, enhancing visibility during imaging. The mice were subsequently transferred to the stage of a two-photon microscope to initiate micropipette insertion. During the in vivo experiments, the two-photon microscope laser power was maintained between 60 and 100 mW, optimizing imaging quality while minimizing photobleaching risks.

686

687

688

690

692

694

696

697

698

699

700

701

703

705

706

707

TABLE II
EVALUATION RESULTS OF THE MICROPIPETTE INSERTION IN IN VIVO

EXP.		1	2	3	4	5
Conv.	TC	1	0	2	2	1
	TL	168.37	157.69	174.97	179.21	167.54
	BD	318.37	157.69	819.80	972.8	427.92
	Time	71.4	45.3	103.2	91.0	72.1
	Blockage	0	0	1	0	0
Ours	TC	0	0	0	0	0
	TL	155.86	155.87	155.86	155.87	155.87
	BD	155.86	155.87	155.86	155.87	155.87
	Time	9.7	10.4	10.4	10.8	10.8
	Blockage	0	0	0	0	0

We evaluated our proposed method against the conventional insertion method. In conventional insertion, the micropipette is advanced axially through the brain tissue, following the focal plane of two-photon imaging. Only lateral or vertical dodging of the pipette is applied when the pipette encounters blood vessels. Figure 10 provides a comparative analysis of the results. Specifically, Fig. 10(a) shows the 3D reconstruction of the micropipette and surrounding vasculature, captured after pipette insertion using the proposed trajectory method. Fig. 10(b) shows the five different navigation potential fields generated by our proposed method for guiding micropipette insertion into the mouse brain. Figure 10(c) and (d) depict the trajectory length and positional error over time for each of the two methods, respectively. Supplementary Fig. S8 further illustrates the trajectory of the micropipette as it traverses from the initial position to the intended depth. These results indicate that the proposed method successfully navigates the micropipette to the target location with improved accuracy and operational efficiency in comparison to the passive approach. Table II shows the statistical evaluation results with TC, TL, brain damage (BD), Time, and blockage. The BD is quantified as being proportional to the CSA of tissue disruption induced by micropipette insertion, serving as an indicator of the spatial extent of mechanical trauma. The metric incorporates the affected tissue cross-section area associated with both nonaxial and axial pipette movements (Supplementary Fig. S3). The Blockage metric evaluates the frequency and range of pipette obstructions encountered during the insertion process. Our proposed approach demonstrates superior performance by maintaining a TC of zero throughout the insertion process, ensuring a smooth and direct path to the target destination. Additionally, it achieves minimal Trajectory Length (TL), which contributes to reduced insertion time. Furthermore, our method causes minimal BD, which lowers tissue disturbance. In contrast, the conventional approach exhibits significantly higher TC and TL values due to its reliance on passive navigation strategies, which often result in less efficient and more convoluted paths. These convoluted trajectories not only

806 807

808

809

811

812

813

814

815

816

817

819

820

821

822

824

825

826

827

829

830

831

832

833

834

835

836

837

838

839

840

841

842

844

845

846

847

849

850

851

852

854

855

856

857

858

859

860

861

862

864

865

867

868

869

870

871

872

874

875

876

877

prolong the insertion time but also lead to increased BD, exacerbating tissue deformation and potential damage. The comparative results underscore the efficiency of our proposed method.

745

747

748

750

751

752

753

754

755

757

758

759

761

763

765

767

768

769

771

772

774

775

776

777

778

779

780

781

782

783

784

785

786

787

788

789

790

791

792

793

794

795

796 797

798

799

800

801

## V. CONCLUSION

This paper introduces an innovative trajectory planning method to actively avoid cerebrovascular structures during micropipette insertion into a highly constrained brain environment. Initially, a feasible navigation space for the micropipette is proposed by incorporating spatial information and micromanipulator motion constraints within the imaging field of a twophoton microscope. Next, the trajectory potential field is then proposed to facilitate precise navigation within this navigation space, optimizing the micropipette's trajectory to reach the desired target depth. The proposed method has undergone both experimental validation and application, demonstrating its effectiveness and efficiency as a proactive trajectory planning algorithm for minimally invasive procedures. Although the proposed method effectively addresses obstacle avoidance during micropipette insertion, there are areas for improvement. Specifically, the feasible navigation space is largely based on the deep-learning segmentation, which relies on substantial GPU resources, highlighting an opportunity for optimization in computational efficiency. Additionally, the trajectory potential field relies on the feasible navigation space, scenarios with a high density of vessels (less than 20% feasible region in navigation space) would pose a challenge to our approach (Supplementary Fig. S6 and S7). The near-saturating vessel would cause the trajectory potential field of our method to be saturated and bleached. In such cases, we recommend abandoning this area and selecting another region for micropipette insertion. Currently, this study focuses primarily on vessel avoidance in micropipette insertion for in vivo patch clamp. Future work could extend to exploring trajectory planning for the entire recording process.

#### ACKNOWLEDGMENT

All necessary craniotomy surgery and experimental procedures involving mice were performed in line with the institutional and ethical guidelines for animal welfare and have been approved by the Institutional Animal Care and Use Committee (IACUC) of Nankai University.

## REFERENCES

- [1] A. C. Bergs *et al.*, "All-optical closed-loop voltage clamp for precise control of muscles and neurons in live animals," *Nature communications*, vol. 14, no. 1, p. 1939, 2023.
- [2] D. Vandael et al., "Subcellular patch-clamp techniques for single-bouton stimulation and simultaneous pre-and postsynaptic recording at cortical synapses," Nature Protocols, vol. 16, no. 6, pp. 2947–2967, 2021.
- [3] S. Ghatak *et al.*, "Single-cell patch-clamp/proteomics of human alzheimer's disease ipsc-derived excitatory neurons versus isogenic wild-type controls suggests novel causation and therapeutic targets," *Advanced Science*, vol. 11, no. 29, p. 2400545, 2024.
- [4] A. Obergrussberger *et al.*, "The suitability of high throughput automated patch clamp for physiological applications," *The Journal of Physiology*, vol. 600, no. 2, pp. 277–297, 2022.
- [5] K. R. Rosholm et al., "Perforated whole-cell recordings in automated patch clamp electrophysiology," Patch Clamp Electrophysiology: Methods and Protocols, pp. 93–108, 2021.

- [6] Q. Zhao et al., "Robotic patch clamp based on noninvasive 3-d cell morphology measurement for higher success rate," *IEEE Transactions* on *Instrumentation and Measurement*, vol. 71, pp. 1–12, 2022.
- [7] H.-J. Suk et al., "Advances in the automation of whole-cell patch clamp technology," *Journal of neuroscience methods*, vol. 326, p. 108357, 2019
- [8] A. Noguchi et al., "In vivo whole-cell patch-clamp methods: recent technical progress and future perspectives," Sensors, vol. 21, no. 4, p. 1448, 2021.
- [9] F. Seibertz et al., "A modern automated patch-clamp approach for high throughput electrophysiology recordings in native cardiomyocytes," Communications biology, vol. 5, no. 1, p. 969, 2022.
- [10] S. B. Kodandaramaiah et al., "Automated whole-cell patch-clamp electrophysiology of neurons in vivo," Nature methods, vol. 9, no. 6, pp. 585–587, 2012.
- [11] B. Long *et al.*, "3d image-guided automatic pipette positioning for single cell experiments in vivo," *Scientific reports*, vol. 5, no. 1, p. 18426, 2015.
- [12] L. A. Annecchino *et al.*, "Robotic automation of in vivo two-photon targeted whole-cell patch-clamp electrophysiology," *Neuron*, vol. 95, no. 5, pp. 1048–1055, 2017.
- [13] H.-J. Suk et al., "Closed-loop real-time imaging enables fully automated cell-targeted patch-clamp neural recording in vivo," Neuron, vol. 95, no. 5, pp. 1037–1047, 2017.
- [14] K. Koos et al., "Automatic deep learning-driven label-free image-guided patch clamp system," *Nature Communications*, vol. 12, no. 1, p. 936, 2021.
- [15] B. Ma et al., "Robotic fast dual-arm patch clamp system for mechanosensitive excitability research of neurons," *IEEE Transactions* on Biomedical Engineering, 2024.
- [16] M. C. Yip et al., "Patch-walking, a coordinated multi-pipette patch clamp for efficiently finding synaptic connections," eLife, vol. 13, p. RP97399, 2024.
- [17] K. Li et al., "Robotic patch clamp electrophysiological signal measurement in multiple brain regions based on brain slice registration," *IEEE Transactions on Automation Science and Engineering*, 2023.
- [18] C. Miranda et al., "Automated microscope-independent fluorescence-guided micropipette," Biomedical Optics Express, vol. 12, no. 8, pp. 4689–4699, 2021.
- [19] Z. Zhang et al., "Robotic micromanipulation: Fundamentals and applications," Annual Review of Control, Robotics, and Autonomous Systems, vol. 2, no. 1, pp. 181–203, 2019.
- [20] G. V. Gonzalez et al., "Robotic automation of "blind" and two-photon targeted patch-clamp electrophysiology in vivo," Authorea Preprints, 2023
- [21] W. A. Stoy et al., "Robotic navigation to subcortical neural tissue for intracellular electrophysiology in vivo," *Journal of Neurophysiology*, vol. 118, no. 2, pp. 1141–1150, 2017.
- [22] S. B. Kodandaramaiah et al., "Multi-neuron intracellular recording in vivo via interacting autopatching robots," Elife, vol. 7, p. e24656, 2018.
- [23] N. S. Desai et al., "Matlab-based automated patch-clamp system for awake behaving mice," *Journal of neurophysiology*, vol. 114, no. 2, pp. 1331–1345, 2015.
- [24] L. Li *et al.*, "A robot for high yield electrophysiology and morphology of single neurons in vivo," *Nature communications*, vol. 8, no. 1, p. 15604, 2017.
- [25] L. Wei et al., "Coarse-to-fine learning for multi-pipette localisation in robot-assisted in vivo patch-clamp," arXiv preprint arXiv:2504.01044, 2025
- [26] F. Feng et al., "Two-photon fluorescence imaging," in Optical Imaging in Human Disease and Biological Research, X. Wei et al., Eds. Singapore: Springer, 2021, pp. 45–61.
- [27] J. Li et al., "Hiswin ut: Hybrid swin transformers network for segmenting 3d in vivo two-photon images of rodent cerebrovasculature," in 2023 IEEE International Conference on Bioinformatics and Biomedicine (BIBM). IEEE, 2023, pp. 2048–2052.
- [28] S. Katoch et al., "A review on genetic algorithm: past, present, and future," Multimedia tools and applications, vol. 80, no. 5, pp. 8091– 8126, 2021.
- [29] J. Ávila et al., "Evaluation of geometric tortuosity for 3d digitally generated porous media considering the pore size distribution and the a-star algorithm," Scientific reports, vol. 12, no. 1, p. 19463, 2022.
- [30] H. Pu et al., "A 3d-rrt-star algorithm for optimizing constrained mountain railway alignments," Engineering Applications of Artificial Intelligence, vol. 130, p. 107770, 2024.
- [31] M. I. Todorov *et al.*, "Machine learning analysis of whole mouse brain vasculature," *Nature Methods*, vol. 17, no. 5, pp. 1–8, 2020.